remote sensing

MDPI

Technical Note

Polarimetric Measures in Biomass Change Prediction Using ALOS-2 PALSAR-2 Data

Henrik J. Persson * and Ivan Huuva

Department of Forest Resource Management, Swedish University of Agricultural Sciences, 901 83 Umeå, Sweden
* Correspondence: henrik.persson@slu.se

Abstract: The use of multiple synthetic aperture radar polarizations can improve biomass estimations compared to using a single polarization. In this study, we compared predictions of aboveground biomass change from ALOS-2 PALSAR-2 backscatter using linear regression based on (1) the cross-polarization channels, (2) the co- and cross-polarizations from fully polarimetric SAR, (3) Freeman–Durden polarimetric decomposition, and (4) the polarimetric radar vegetation index (RVI). Additionally, the impact of forest structure on the sensitivity of the polarimetric backscatter to AGB and AGB change was assessed. The biomass consisted of mainly coniferous trees at the hemi-boreal test site Remningstorp, located in southern Sweden. We found some improvements in the predictions when quad-polarized data (RMSE = 79.4 tons/ha) were used instead of solely cross-polarized data (RMSE = 84.9 tons/ha). However, when using Freeman–Durden decomposition, the prediction accuracy improved further (RMSE = 69.7 tons/ha), and the highest accuracy was obtained with the radar vegetation index (RMSE = 50.4 tons/ha). The corresponding R^2 values ranged from 0.45 to 0.82. The bias was less than 1 t/ha for all models. An analysis of forest variables showed that the sensitivity to AGB was reduced for high values of basal-area-weighted mean height, basal area, and stem density when predicting absolute AGB, but the best change prediction model was sensitive to changes larger than the apparent saturation point for AGB state estimates. We conclude that by using fully polarimetric SAR images, forest biomass changes can be estimated more accurately compared to using single- or dual-polarization images. The results were improved the most (in terms of RMSE and R^2) by using the Freeman–Durden decomposition model or the RVI, which captured especially the large changes better.

Keywords: biomass change; SAR; backscatter; polarimetry; forestry

Citation: Persson, H.J.; Huuva, I. Polarimetric Measures in Biomass Change Prediction Using ALOS-2 PALSAR-2 Data. *Remote Sens.* **2024**, *16*, 953. https://doi.org/10.3390/rs16060953

Academic Editors: Armando Marino and Michele Martone

Received: 28 December 2023
Revised: 22 February 2024
Accepted: 7 March 2024
Published: 8 March 2024

1. Introduction

Ecosystems are undergoing significant transformations because of climate change, deforestation, and land-use alterations, necessitating accurate and efficient methods for monitoring and quantifying changes in terrestrial vegetation. Understanding these changes is of high importance, as terrestrial vegetation (in this paper, quantified in terms of aboveground biomass (AGB)), plays a critical role in carbon cycling, biodiversity preservation, and overall ecosystem health. Accurate estimation of AGB change is not only essential for ecological studies, but also has far-reaching implications for climate change mitigation and sustainable resource management. Traditional field-based inventories, sometimes in combination with optical remote sensing methods, have long been used to assess AGB change. Yet, field inventories have limited information on the spatial distribution, and optical satellite sensors are limited by factors such as light conditions, cloud cover, atmospheric interference, and the saturation of dense forested areas. In contrast, synthetic aperture radar (SAR) has emerged as a useful sensor for overcoming these limitations. SAR sensors provide valuable insights into the structural and dielectric properties of vegetation canopies, making them particularly well suited for monitoring AGB change in diverse and challenging environments. The impact of wavelength on AGB estimations in SAR remote

sensing is crucial, and the use of L-band SAR offers certain advantages. At longer wavelengths (e.g., L-band), SAR can penetrate vegetation canopies more effectively compared to shorter wavelengths like X-band or C-band, which, consequently, interact to a higher degree with the top part of the canopy. At the same time, the penetration at the L-band is mainly limited to within-canopy scattering, hence reducing the disturbance from scattering due to topography, therefore being particularly advantageous for AGB estimations [1–7].

Yet, with increasing canopy density and AGB, SAR backscatter has been reported to also saturate at the L-band [8,9]. The AGB level at which loss of sensitivity has been reported to occur is dependent on the wavelength and forest type, and has been seen to occur already at 50 tons/ha in ALOS PALSAR L-band data over a Eucalyptus forest, corresponding to a plantation age of 3 years, and at various levels ranging from 40 tons/ha to 100 tons/ha for the L-band in conifer-dominated forests [10–16].

The physical mechanism of the reported loss of sensitivity with increasing AGB is complex, and it seems like changes in some structural properties with age tend to decrease the backscatter (e.g., decreasing stem numbers and increasing heights), but changes in other forest structural variables actually increase the backscatter with stand maturity (e.g., increasing stem sizes) [9], leading to a close-to-net-zero change in backscatter at a certain stage of maturity or level of AGB. Smith-Jonforsen et al. [17] noted a related effect in electromagnetic modeling and field measurements, where it was noted that the stem density greatly affected P-band backscatter for constant AGB. Additionally, it seems like varying ground contributions due to local topography may confound the backscatter from biomass [4]. It is conceivable that these competing properties could be partially separated via different polarimetric scattering signatures, which could facilitate AGB change estimation beyond the so-called backscatter saturation points observed in the literature.

Fully polarimetric data are needed to characterize SAR backscattering completely, i.e., a SAR that transmits and receives signals with two orthogonal polarization states. Still, scattering from natural targets like forests is stochastic, and target decomposition theorems attempt to express the dominating scattering mechanisms [18,19]. The most common orthogonal basis set used in SAR sensors comprises horizontal (H) and vertical (V) polarizations, which allow measurements of both co-polarized transmit and receive signals (HH and VV) and cross-polarized signals (VH and HV). However, adding polarimetric channels to SAR comes with the tradeoff that the spatial resolution and swath width are normally reduced. In conventional strip map SAR imaging, fully polarimetric operation either reduces the pulse repetition frequency PRF per channel, thus reducing the unambiguous Doppler shift range, which reduces the attainable azimuth resolution, or increases the total PRF, which reduces the attainable swath width [20,21]. Furthermore, fully polarimetric SAR systems often require larger or more complex antennas to accommodate multiple polarization channels, and also have a reduced signal-to-noise ratio (SNR) for each polarization channel when compared to single or dual polarization modes, thus reducing the radiometric resolution.

The use of PolSAR data for the estimation of AGB has been analyzed to varying degrees in different forest types. The backscatter in separate polarizations and different decompositions has been analyzed in tropical [22–25] and temperate [26] forests using airborne or satellite data. Authors have also reported the loss of backscatter sensitivity to biomass over certain amounts, proposed polarimetric decompositions, interferometry, and tomography as means to overcome the issue, and acknowledged the need for ground backscatter suppression [22,23,27,28]. A few studies have focused on the Freeman–Durden (FD) decomposition of airborne or satellite-borne SAR data applied to boreal forest [29–31]. Of these, Antropov et al. [30] has most extensively explored PolSAR with a modified FD model to classify pixels due to the dominant volume scattering mechanism for boreal forest in Finland, hence its relevance for AGB estimation in Sweden. In Swedish boreal forest, Sandberg et al. [32] investigated the use of airborne E-SAR P-band SAR for estimating AGB changes. Additionally, Huuva et al. [33] and Huuva et al. [34] investigated fully polarimetric L-band data for AGB change estimation. The latter two studies used airborne

data from the E-SAR and SETHI systems, and PALSAR-2 data, respectively. The benefit of using multiple polarizations was assessed, but as only the individual polarization channels were used as predictors in AGB change models, no polarimetric decompositions were investigated.

Various polarimetric SAR models using airborne and satellite-borne data have been investigated for forest applications, but we restricted our scope of decomposition models to the FD model, which is well established and especially developed to describe forest scattering [30,35–40]. The FD decomposition technique fits a three-component scattering model based on the physics of radar scattering to polarimetric SAR observations [36]. The three scattering mechanisms in the FD model are Bragg scattering for moderately rough surfaces, even-bounce scattering from a pair of orthogonal surfaces with different dielectric constants, and volume scattering from a cloud of randomly oriented dipoles. The FD volume component was shown to be most strongly related to AGB among a number of polarimetric attributes in ALOS PALSAR images [41], and seen to be suitable for analyzing natural distributed targets, and to differentiate well between vegetation types [42].

In addition to formal decompositions, a non-linear combination of the cross- and co-polar channels, i.e., the radar vegetation index (RVI), was proposed by Kim and van Zyl [43] to describe the relative strength of vegetation scattering. RVI has been used extensively to obtain both biomass and vegetation water content, and is correlated with shrubland, crop, and forest vegetation [41,44–47]. Among L-band polarization channels, the correlation with both AGB and AGB change in boreal forests has been observed to be the highest for HV (or VH) [33,34]. RVI is essentially the ratio of cross-polarized backscatter power to total backscattered power, and the ratios of polarized channels appear to be less sensitive to topography, viewing geometry, and calibration errors compared to the additive use of polarized channels [4,32,33].

The objectives of this study, all adressing L-band SAR in a boreal forest, were to: (1) assess if the use of multiple polarizations could improve AGB change estimates compared to a single polarization, (2) compare different polarimetric SAR approaches for estimating AGB change, (3) identify if saturation effects can be reduced or overcome by using multiple polarizations, and (4) investigate the impact of forest structure on the sensitivity of L-band polarimetric backscatter to AGB and AGB change.

2. Materials and Methods

2.1. Test Site

The test site, Remningstorp, is located in southern Sweden (58°30′N 13°40′E), consisting of about 1200 ha of commercially managed hemi-boreal forest (Figure 1a). About two-thirds of the forest grows on till, a mixture of glacial debris with a field layer of herbs, blueberry (*Vaccinium myrtillus* L.), and narrow-leaf grass (e.g., *Deschampsia flexuosa* (L.) Trin.). The main tree species are Norway spruce (*Picea abies* (L.) H. Karst.), Scots pine (*Pinus sylvestris* L.), and birch (*Betula* spp.). The landscape is mainly flat with smaller slopes, with the elevations ranging from 120 m to 145 m above sea level.

2.2. Field Data

Forty-six field plots with a 40 m radius were subjectively distributed across the test site (Figure 1b) with the aim of establishing a spatially well-spread-out sample roughly representative of the test area in terms of tree species and age. They were field surveyed after the growth season of 2014, and again after the growth season of 2021. All trees with a diameter at breast height (DBH, measured at 1.3 m above ground) of more than 4 cm were calipered, the species was registered and positioned using a real-time kinematic global positioning system. The height was measured on a subsample of trees with a hypsometer. These height-measured trees were randomly selected from each plot with a probability proportional to their basal area. Aboveground biomass (AGB) was estimated using allometric models by Marklund [48]. Lorey's height, i.e., the basal-area-weighted mean height (h_L), basal area (BA), and stem density (n, number of stems/ha) were computed plot-wise. For

seven plots containing young forest, n was estimated using a linear model relating n to AGB using data from the remaining plots. The majority tree species was defined as the tree species with proportionally the highest AGB in 2014 per plot.

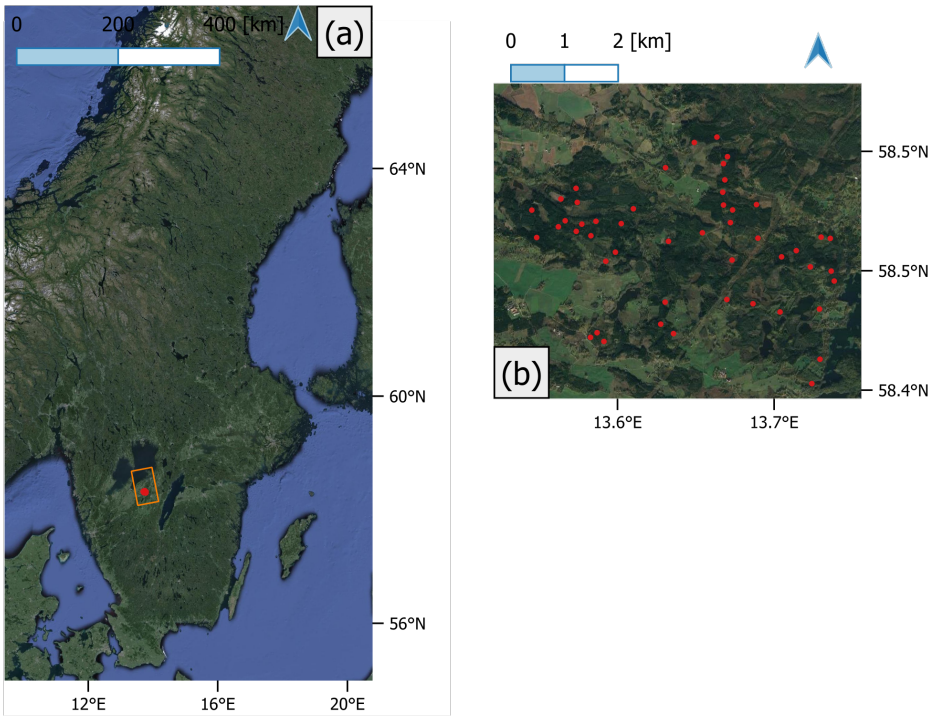

Figure 1. (**a**) Extent of satellite scene in orange and location of test site, Remningstorp, in red. (**b**) Plot locations of the 46 field plots in red.

2.3. Laser Data

A national terrain model was provided as a raster by the Swedish National Land Survey with 2 × 2 m pixels. It was derived from ground-classified airborne laser scanning data, acquired in 2018, with 1–2 points/m^2.

2.4. SAR Data

This study used two ALOS-2 PALSAR-2 fully polarimetric data in highly sensitive stripmap mode (Table 1). The acquisitions were selected from the same track and with the same ascending orbital direction to avoid changes in backscatter due to acquisition geometry. The data were delivered in slant range geometry in Single Look Complex (SLC) format.

Table 1. ALOS-2 PALSAR-2 scenes used in this study.

Acquisition Date	Off-Nadir Angle	Resolution	Mode	Observation Direction	Orbit	Time	Weather
11 June 2015	28.4°	6 m	HBQ	Right-looking	Asc	22:37	0 mm, 13 °C, 4 m/s
3 June 2021	28.4°	6 m	HBQ	Right-looking	Asc	22:37	0 mm, 17 °C, 4 m/s

2.5. Modeling

The biomass change was estimated directly rather than estimating the state of biomass at two times followed by computing the difference [49,50]. Furthermore, we decided to include the predictors in a pairwise manner, meaning that they should be present at both t1 and t2, and they were used without deriving the difference of each predictor [50]. For all

models, we used linear regression to estimate the model parameters, and the models had the form

$$\Delta AGB = \alpha_0 + \alpha_1 p_1 + \cdots + \alpha_k p_k + \epsilon, \quad (1)$$

where ΔAGB denotes the AGB change from 2015 to 2021, and α_i ($i = 0, 1, 2 \ldots, k$) denote the model parameters to be estimated. The parameters consist of an intercept term α_0 and a coefficient for each of the k predictors. ϵ denotes the residual model error. For each model, a type of predictor (say $\overline{\gamma}^0_{HV}$) was kept in the final models if, at least for one of the acquisition dates, the predictor was significant (t-test at a 5% significance level). We compared four different models, where the first, most straightforward model used the mean of the cross-polarizations (HV + VH)/2 (assuming reciprocity—and decreasing the noise by averaging) as predictors in (1). Cross-polarization data typically have a lower signal-to-noise (SNR) ratio than co-polarizations, while at the same time, often have shown a stronger correlation to AGB. Using only the cross-polarizations in a fully polarized SAR image may underestimate the performance compared to using the cross-polarization in a dual-polarized SAR image, due to the decreased SNR as a consequence of capturing all polarizations. The noise-equivalent-sigma-zero (NESZ) changes from −28 dB to −25 dB, when working on fully polarimetric PALSAR-2 data instead of single- or dual-polarimetric PALSAR-2 data (https://www.eorc.jaxa.jp/ALOS-2/en/about/palsar2.htm, accessed on 6 September 2023), but no suitable single- or dual-polarimetric scenes were available for the approximate time points. The second model extended the first with the co-polarizations VV and HH. The third model used the Freeman–Durden decomposition model to derive three scattering components representing canopy scatter (vol) from randomly oriented dipoles—e.g., forest—even- or double-bounce scattering from a pair of orthogonal surfaces with different dielectric constants (dbl), and Bragg scatter from a moderately rough surface (surf), which were used as predictors in (1). FD decomposition has been tested for various forest applications, but rarely in boreal forest and not for the estimation of AGB change. The fourth model used the radar vegetation index, defined as [43]

$$RVI = \frac{8\gamma^0_{HV}}{\gamma^0_{HH} + \gamma^0_{VV} + 2\gamma^0_{HV}}, \quad (2)$$

where γ^0 (gamma-nought) represents the radiometrically and geometrically corrected SAR backscattering coefficients of the polarization channels, with subscripts denoting the channel. RVI is the ratio of the cross-polarized power to total power. It generally, but not strictly, ranges between 0 and 1, and can be seen as a measure of scattering randomness. Being a ratio, RVI has less sensitivity to radar measurement geometry and topography, and is also insensitive to absolute calibration errors. The candidate predictors (subscripted with the acquisition year) that were tested for the first model were $\overline{\gamma}^0_{HV15}$, γ^0_{VV15}, γ^0_{HH15}, $\overline{\gamma}^0_{HV21}$, γ^0_{VV21}, and γ^0_{HH21}, and for the second model, the following predictors were tested: $vol_{15}, dbl_{15}, surf_{15}, vol_{21}, dbl_{21}, surf_{21}$. The bar over $\overline{\gamma}^0_{HVXY}$ indicates the cross-polarized average. Out of these candidate predictors, the ones selected using the above procedure were kept in the final models. The significant (i.e., included) predictors of the final models and their estimated coefficients are listed in Table 2.

Table 2. Included predictors and estimated regression coefficients in the final AGB change models. All models include an intercept term with the coefficient α_0. Predictor subscripts include the acquisition year (15 = 2015, 21 = 2021).

Model	Predictors	α_0	α_1	α_2	α_3	α_4	α_5
1	$\overline{\gamma}^0_{HV15}, \overline{\gamma}^0_{HV21}$	170	−26.2	37.8			82.8
2	$\overline{\gamma}^0_{HV15}, \gamma^0_{VV21}, \overline{\gamma}^0_{HV21}, \gamma^0_{VV21}$	33.5	−29.0	11.1	56.8	−53.1	74.1
3	$surf_{15}, surf_{21}$	−122.5	16.1	−25.2			65.7
4	RVI_{15}, RVI_{21}	−58.6	−34,880	52,016			47.8

To assess the potential impacts of forest structure, we also created scatter plots of the best performing model (in terms of RMSE and R^2) where the points (illustrated in different colors) represented different ranges of field-inventoried variables. We focused on h_L, BA, and n as these were proposed and investigated by Joshi et al. [9]. 208 While the quantitative investigation concerns the prediction of AGB change, the state of AGB in 2015 was also modeled. This was carried out in order to illustrate the relationship between AGB and SAR data, and to support the interpretation of saturation effects. This was achieved using models 1–4, including all candidate predictors, whether or not the predictors were significant, but replacing AGB change with AGB as the response variable.

2.6. SAR Processing

The SAR images were processed in SNAP (Sentinel Application Platform v 9.0.0) following the same procedure as for the 2015 and 2021 images. Three SAR processing workflows were developed to generate the predictors at 10 m pixels for the different models described in the previous section.

The first workflow derived the backscatter γ^0 for each polarization as follows: radiometric calibration; speckle filtering using Lee-Sigma with a window size of 17 × 17 pixels, a target window of 3 × 3 pixels, and sigma = 0.9; multilooking (2 × 4 pixels in range and azimuth, respectively) [51]; and finally, geometric correction by using the national DTM followed by resampling the output to a 10 m grid.

The second workflow derived the Freeman–Durden-decomposed components: radiometric calibration; polarimetric-speckle-filtering using Improved Lee-Sigma with a window size of 17 × 17 pixels, a target window of 3 × 3 pixels, and sigma = 0.9; polarimetric Freeman–Durden decomposition (window size of 17 × 17 pixels); multilooking (2 × 4 pixels in range and azimuth, respectively); and finally, geometric correction by using the national DTM followed by resampling the output to a 10 m grid.

The third workflow was used to compute the radar vegetation index (RVI), which was derived using the polarimetric parameter function in SNAP: radiometric calibration, computation of RVI in a 5 × 5 pixel window, and geometric correction by using the national DTM followed by resampling the output to a 10 m grid.

2.7. Validation

Leave-one-out cross-validation (LOOCV) was used to to validate the method, meaning that one plot was left out, while the remaining plots were used to estimate the model parameters. The estimated model was then used to predict on the left-out plot and quantify the model prediction error. The procedure was repeated until all plots were predicted on. The prediction quality was estimated with the root mean square error (3) and bias (4) of cross-validated predictions as

$$RMSE = \sqrt{\frac{\sum_{n=1}^{N}(\hat{y}_i - y_i)^2}{N}}, \text{and} \tag{3}$$

$$Bias = \frac{\sum_{n=1}^{N}(\hat{y}_i - y_i)}{N}, \tag{4}$$

where $\hat{y}_i$ is the prediction for plot i, y_i is the corresponding reference value, and N is the number of field plots.

3. Results and Discussion

All models captured the overall trend relatively well (Figure 2), although it can be disadvantageous to use a single model for both forest growth and large decreases in forest. The RMSE decreased for every model, from 84.9 tons/ha for the first model to 50.4 tons/ha for the fourth model (Table 3). The added information in terms of polarization (model 2) and the additional weighting of different scattering mechanisms (models 3 and 4) provided complementary information, which decreased the variance. The bias was small to moderate

for all four of our models (Table 3). Both model three, based on FD decomposition, and model four (RVI), based on non-linear weighting of the different polarizations, decreased the variance, in particular for the clear-cut plots. This indicates that they reflect the change in dominating scattering type better than the direct use of cross- and co-polarizations, which was obviously most distinct for the clear-cut plots. Yet, the variance for the plots indicating growth was considerable in all four models. No strong relation to tree species was noticed, although Joshi et al. [9] pointed out that this was one driving factor for the varying response in the HH and HV channels. However, systematic errors (e.g., effects due to tree species) can be concealed in change estimates, since the same errors could appear at both measurement times. This differs from models estimating the state. The fourth model (based on RVI) showed the lowest overall RMSE (50.4 tons/ha), a percentage point error reduction of 41 compared to model one, and the highest coefficient of determination (0.82). It used contributions from all three observed polarizations involved in the model, which appears to have captured complementary information compared to models 1–3. No clear saturation point in terms of maximum absolute AGB change predicted was observed for the model. This confirms earlier results where AGB decreases of 300 t/ha were predicted using fully polarimetric airborne L-band data [33]. Yet, the variance around the 1:1 line is considerable for all models, and different models may be preferred for the prediction of different types of changes, e.g., the currently investigated models can be suitable to predict larger forest declines, while forest growth may be better captured using a separate set of models.

Table 3. AGB change prediction results from the plot-level cross-validation.

Model	RMSE (tons/ha)	Bias (tons/ha)	R^2	N
1	84.9	−0.795	0.45	46
2	79.4	−0.245	0.58	46
3	69.7	0.662	0.65	46
4	50.4	0.391	0.82	46

Joshi et al. [9] stressed that forest structure has an impact on the SAR backscatter intensity. We therefore grouped the field plots based on the same forest structure variables (2014 field inventory) that Joshi et al. highlighted (Figure 3). It seems that the plots with the largest h_L agree best with the overall model, while the plots with smallest h_L caused larger residuals (Figure 3a). For BA (Figure 3b), no clear relationships were identified, and the effect of stem density (Figure 3c) did not provide any clear insights. The impact of forest structure was further investigated for the AGB (state) estimates to see if it was similar.

The scatter plots of modeled AGB for 2014 (Figure 4) provide the possibility to infer what the polarimetric components of the models capture. The largest difference is between model one, based on cross-polarization, and the remaining multi-polarization models. The differences between models 3 and 4 are small, and more plots or larger field plots or additional structure attributes capturing other aspects appear necessary to explain the differences further. Model 3 appears to have a more distinct upper limit than the other models (Figure 4c). The sensitivity to AGB was very poor across the whole range when only cross-polarization was used, possibly due to a higher noise level (Figure 4a), while it was possibly not reached when all polarizations were used (Figure 4b), although the slope started to decrease. While models 3 and 4 appeared best for the estimation of AGB change, this was not as apparent for AGB estimates. The saturation point was shifted upwards by adding more polarizations, with the highest saturation point around 200 tons/ha, which is higher than the commonly cited 100 tons/ha for the L-band. The use of multi-temporal data has also been shown to give significant improvements in this aspect [52].

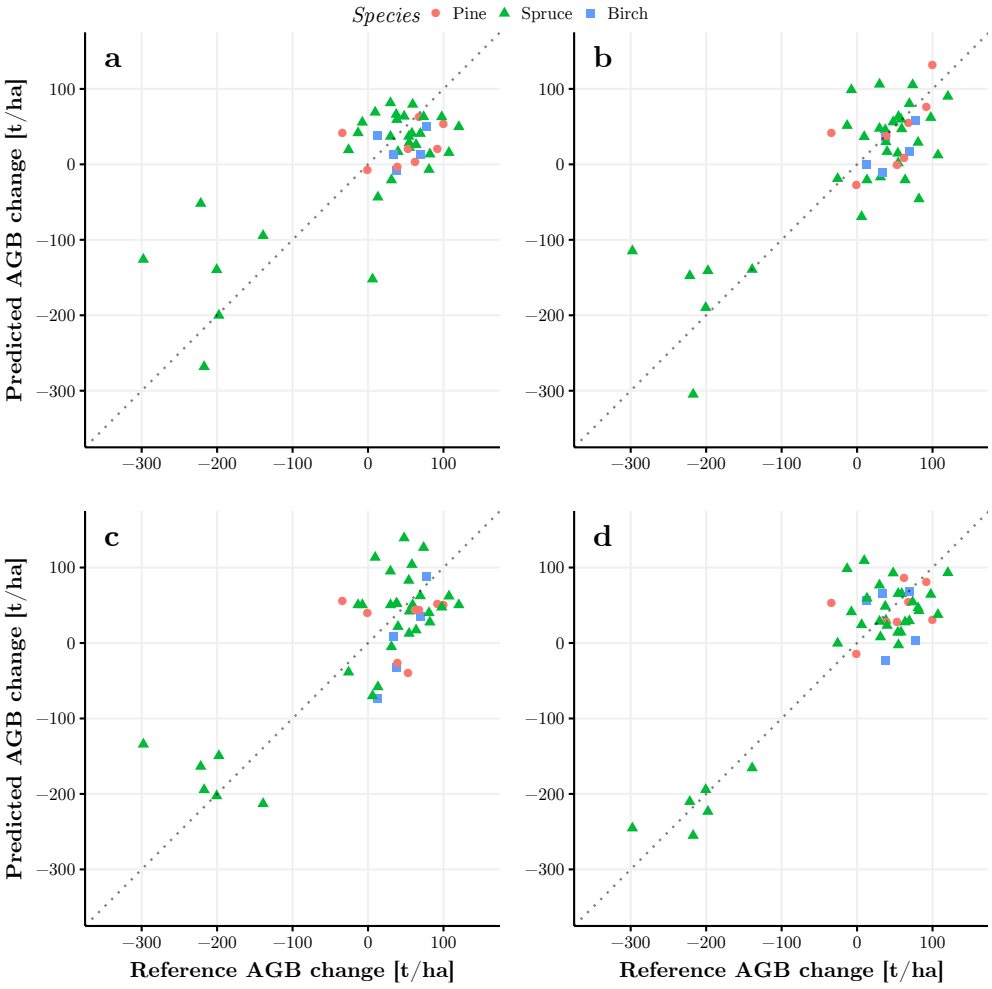

Figure 2. Scatter plots of predicted vs. reference (field) AGB change between 2015 and 2021. (**a**) Model 1—based on cross-polarization. (**b**) Model 2—based on cross- and co-polarizations. (**c**) Model 3—Freeman–Durden-based. (**d**) Model 4—RVI-based.

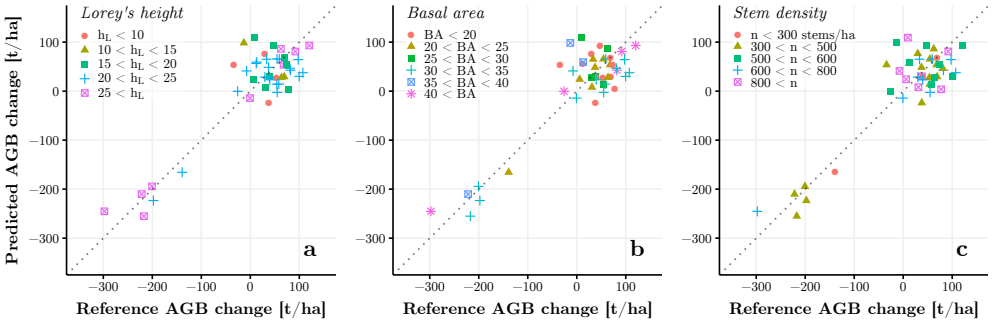

Figure 3. Scatter plots of predicted vs. reference (field) AGB change for model 4—RVI—with colors representing different ranges of structure variables. (**a**) Lorey's height, (**b**) basal area, (**c**) stems per hectare. Values of structure variables are from the 2014 survey.

The scatter plots of AGB with different colors for the different h_L, BA, and n (Figure 5a–c) indicate some clusters of plots, in particular for h_L and BA. Plots with larger h_L were more often underestimated, while plots with smaller h_L were more often overestimated. Beyond an h_L of 20 m, the sensitivity decreased significantly (Figure 5a). BA appeared to be correlated with saturation point, with plots that had a BA < 30 m^2/ha showing a linear relationship (predicted vs. field), and with the BA increasing beyond 30 m^2/ha, this sensitivity to increased AGB diminished or vanished. Analyzing the relationship with

stem density, the correlation between estimated and reference AGB appears weaker above 500 stems/ha (Figure 5c).

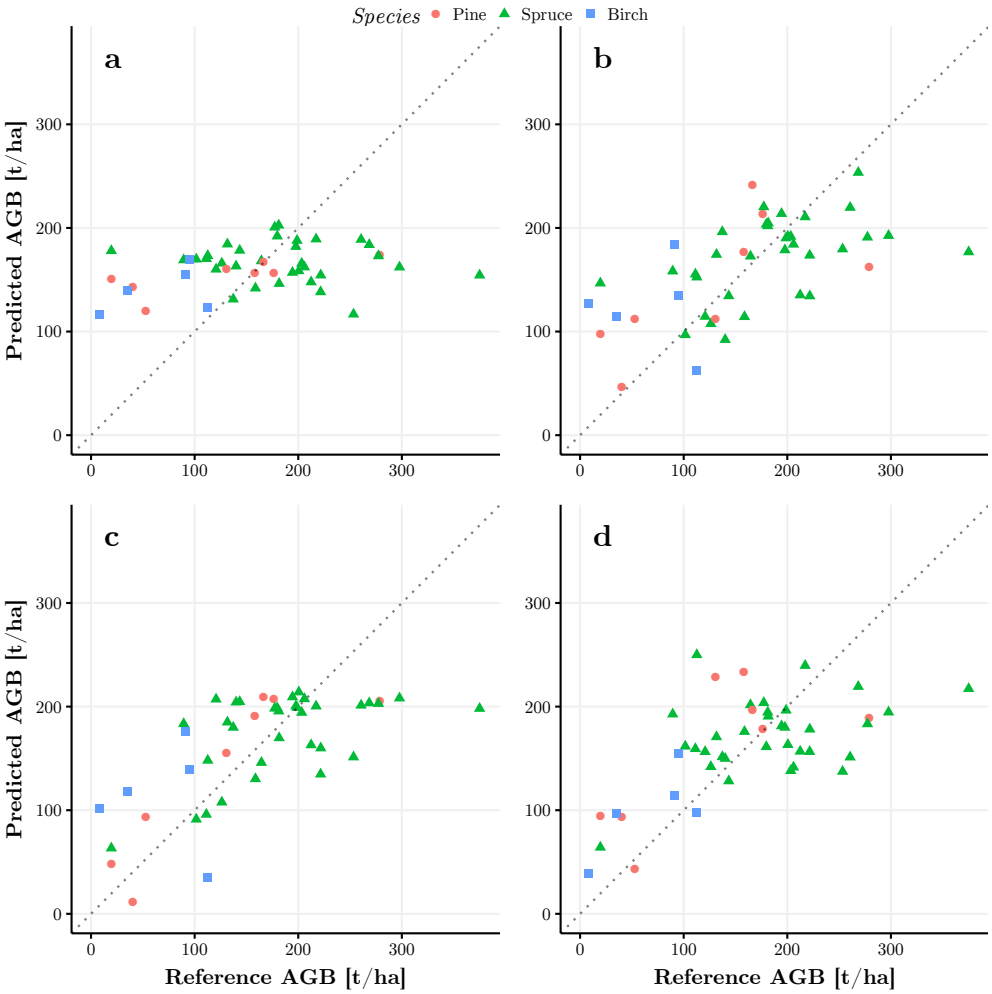

Figure 4. Scatter plots of predicted vs. reference (field) AGB 2014. (**a**) Model 1—based on cross-polarization. (**b**) Model 2—based on cross- and co-polarizations. (**c**) Model 3—Freeman–Durden-based. (**d**) Model 4—based on RVI.

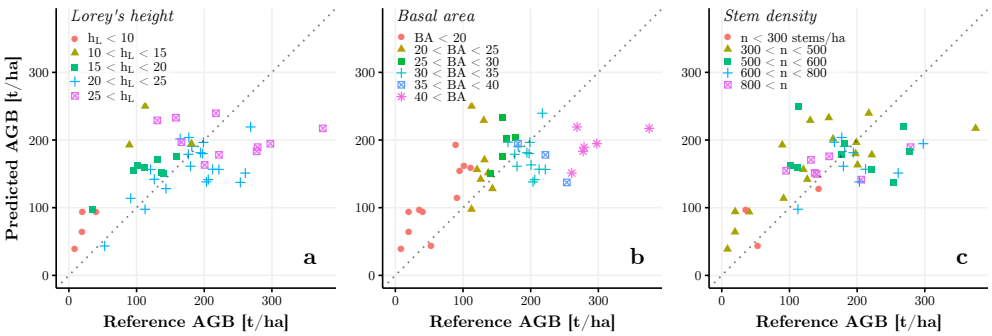

Figure 5. Scatter plots of predicted vs. reference (field) AGB 2014 for model 4—RVI—with colors representing different ranges of structure variables. (**a**) Lorey's height, (**b**) basal area, (**c**) stems per hectare.

Although the volume component in FD is generally the strongest from forest vegetation [35,36], only the surface component of model 3 was significant in predicting both AGB and AGB change. However, the dominant scattering contributions extracted from FD and RVI are most often applied to stratification into land cover classes, not estimation, so

it is not entirely clear which scattering mechanism would best correlate with variations in AGB within a class, which is the focus in this study. A number of decompositions and polarimetric parameters have been proposed, such as the modifications to FD decomposition in Antropov et al. [30], or the generalized radar vegetation index, which has shown improvements compared to the RVI in determining correlations with vegetation water content [53]. These studies try to better capture the dominant scattering contributions from vegetation and improve on the measures used in this study. Promising candidates could in future studies be compared to the measures in this study.

The general noise levels may confound the analysis in this paper, which could be alleviated by using larger field plots, but the plots used in this study were already quite large, and larger inventories are costly, so a more feasible approach could be to estimate the reference AGB and structural variables for even larger homogeneous forest stands using multiple sample plots for each stand, over which the polarimetric analysis could be conducted. On the other hand, further insights about the polarimetric scattering behavior for L-band data in hemi-boreal forests could also be investigated using SAR data of higher spatial and radiometric resolution, i.e., experimental airborne or tower-based SAR data.

The use of interferometric coherence was not assessed in this study, although the relatively low biomass levels in boreal forest provide favourable conditions for adding it as a predictor, which has also appeared useful for repeat-pass satellite SAR configurations at the L-band [54,55]. Generally, the temporal decorrelation over forest has been problematic for interferometric SAR approaches, when repeat-pass configurations are used (as is the case for ALOS-2). Weather aspects were not investigated in this study, although similar precipitation-free conditions were considered for both the 2015 and 2021 images, and the acquisition dates were chosen to agree in terms of phenology. Because of this, the results of this study may not generalize to cases where there are large differences in weather or moisture, or, for example, images acquired in freezing conditions. Indeed, a number of studies have previously noted the strong effect of both moisture and freeze/thaw conditions on backscatter from forests [4,32,33]. In general, SAR backscatter images used for biomass change prediction should be chosen from acquisitions with similar conditions, or differences in backscatter relating to moisture should be somehow corrected for, such as in, for example, Huuva et al. [33].

4. Conclusions

This study investigated how fully polarimetric SAR images acquired at the L-band could be used to estimate aboveground biomass changes. By adding more polarizations or decomposition components as predictors from fully polarimetric data, the variance was reduced and the best results were obtained with the radar vegetation index, with an RMSE of 50.4 tons/ha and with an R^2 of 0.82. Both the Freeman–Durden decomposition and radar vegetation index appeared to reflect the change in the dominating scattering mechanism better than the direct use of cross- and co-polarizations by reducing the errors, particularly for the clear-cut plots. The saturation point for AGB state estimation was shifted slightly upwards by adding more polarizations, with the highest saturation point occurring around 200 tons/ha. No clear correlation between tree species and sensitivity to AGB or AGB change was observed. The sensitivity to AGB was reduced for large values of h_L, BA, and n when predicting absolute AGB, but the best change prediction model was still sensitive to differences in changes larger than the apparent saturation point for AGB state estimates. We conclude that fully polarimetric data are more capable of reflecting biomass changes than single- or dual-polarization data and that while sensitivity to AGB state decreased around 200 tons/ha at our boreal test site, no clear saturation point in terms of the maximum absolute AGB change predicted was observed for the best model using the radar vegetation index. We encourage future studies to further investigate the impact of forest structure and explore the benefits of also using interferometric coherence.

Author Contributions: Conceptualization: H.J.P. and I.H., Methodology: H.J.P. and I.H., Validation: H.J.P. and I.H., Formal Analysis: H.J.P., Investigation: H.J.P. and I.H., Data Curation: H.J.P., Writing—Original Draft: H.J.P. and I.H., Visualization: H.J.P. and I.H., Project Administration: H.J.P., Funding Acquisition: H.J.P. All authors have read and agreed to the published version of the manuscript.

Funding: This project was funded by the Swedish Forest Society Foundation (Skogssällskapet), 2021-923-Steg 2 2020 and 2022-1112-Steg 2 2022.

Data Availability Statement: The data used in this study are available upon reasonable request.

Acknowledgments: The ALOS-2 PALSAR-2 data were provided by JAXA EORC within the 3rd Research Announcement on the Earth Observations (PI: Johan Fransson, ER3A2N096). We thank Maciej Soja for providing constructive feedback, and the Hildur and Sven Wingquist Foundation for their financial support.

Conflicts of Interest: The authors declare no conflicts of interest.

References

1. Woodhouse, I. Predicting backscatter-biomass and height-biomass trends using a macroecology model. *IEEE Trans. Geosci. Remote Sens.* **2006**, *44*, 871–877. [CrossRef]
2. Rosenqvist, A.; Shimada, M.; Ito, N.; Watanabe, M. ALOS PALSAR: A Pathfinder Mission for Global-Scale Monitoring of the Environment. *IEEE Trans. Geosci. Remote Sens.* **2007**, *45*, 3307–3316. [CrossRef]
3. Santoro, M.; Fransson, J.E.S.; Eriksson, L.E.B.; Magnusson, M.; Ulander, L.M.H.; Olsson, H. Signatures of ALOS PALSAR L-Band Backscatter in Swedish Forest. *IEEE Trans. Geosci. Remote Sens.* **2009**, *47*, 4001–4019. [CrossRef]
4. Soja, M.J.; Sandberg, G.; Ulander, L.M.H. Regression-Based Retrieval of Boreal Forest Biomass in Sloping Terrain Using P-Band SAR Backscatter Intensity Data. *IEEE Trans. Geosci. Remote Sens.* **2013**, *51*, 2646–2665. [CrossRef]
5. Rosenqvist, A.; Shimada, M.; Suzuki, S.; Ohgushi, F.; Tadono, T.; Watanabe, M.; Tsuzuku, K.; Watanabe, T.; Kamijo, S.; Aoki, E. Operational performance of the ALOS global systematic acquisition strategy and observation plans for ALOS-2 PALSAR-2. *Remote Sens. Environ.* **2014**, *155*, 3–12. [CrossRef]
6. Joshi, N.P.; Mitchard, E.T.A.; Schumacher, J.; Johannsen, V.K.; Saatchi, S.; Fensholt, R. L-Band SAR Backscatter Related to Forest Cover, Height and Aboveground Biomass at Multiple Spatial Scales across Denmark. *Remote Sens.* **2015**, *7*, 4442–4472. [CrossRef]
7. Santoro, M.; Cartus, O.; Fransson, J.E.S.; Wegmüller, U. Complementarity of X-, C-, and L-band SAR Backscatter Observations to Retrieve Forest Stem Volume in Boreal Forest. *Remote Sens.* **2019**, *11*, 1563. [CrossRef]
8. Avitabile, V.; Herold, M.; Heuvelink, G.B.M.; Lewis, S.L.; Phillips, O.L.; Asner, G.P.; Armston, J.; Ashton, P.S.; Banin, L.; Bayol, N.; et al. An integrated pan-tropical biomass map using multiple reference datasets. *Glob. Chang. Biol.* **2016**, *22*, 1406–1420. [CrossRef] [PubMed]
9. Joshi, N.; Mitchard, E.T.A.; Brolly, M.; Schumacher, J.; Fernández-Landa, A.; Johannsen, V.K.; Marchamalo, M.; Fensholt, R. Understanding 'saturation' of radar signals over forests. *Sci. Rep.* **2017**, *7*, 3505. [CrossRef] [PubMed]
10. Dobson, M.C.; Ulaby, F.T.; Toan, T.L.; Beaudoin, A.; Kasischke, E.S.; Christensen, N. Dependence of radar backscatter on coniferous forest biomass. *IEEE Trans. Geosci. Remote Sens.* **1992**, *30*, 412–415. [CrossRef]
11. Toan, T.L.; Beaudoin, A.; Riom, J.; Guyon, D. Relating forest biomass to SAR data. *IEEE Trans. Geosci. Remote Sens.* **1992**, *30*, 403–411. [CrossRef]
12. Rignot, E.; Way, J.; Williams, C.; Viereck, L. Radar estimates of aboveground biomass in boreal forests of interior Alaska. *IEEE Trans. Geosci. Remote Sens.* **1994**, *32*, 1117–1124. [CrossRef]
13. Imhoff, M.L. Radar backscatter and biomass saturation: Ramification for global biomass inventory. *IEEE Trans. Geosci. Remote Sens.* **1995**, *33*, 511–518. [CrossRef]
14. Fransson, J.E.S.; Israelsson, H. Estimation of stem volume in boreal forests using ERS-1 C- and JERS-1 L-band SAR data. *Int. J. Remote Sens.* **1999**, *20*, 123–137. [CrossRef]
15. Yu, Y.; Saatchi, S. Sensitivity of L-Band SAR Backscatter to Aboveground Biomass of Global Forests. *Remote Sens.* **2016**, *8*, 522. [CrossRef]
16. Baghdadi, N.; Le Maire, G.; Bailly, J.S.; Ose, K.; Nouvellon, Y.; Zribi, M.; Lemos, C.; Hakamada, R. Evaluation of ALOS/PALSAR L-Band Data for the Estimation of *Eucalyptus* Plantations Aboveground Biomass in Brazil. *IEEE J. Sel. Top. Appl. Earth Obs. Remote Sens.* **2015**, *8*, 3802–3811. [CrossRef]
17. Smith-Jonforsen, G.; Folkesson, K.; Hallberg, B.; Ulander, L.M.H. Effects of Forest Biomass and Stand Consolidation on P-Band Backscatter. *IEEE Geosci. Remote Sens. Lett.* **2007**, *4*, 669–673. [CrossRef]
18. Cloude, S.; Pottier, E. A review of target decomposition theorems in radar polarimetry. *IEEE Trans. Geosci. Remote Sens.* **1996**, *34*, 498–518. [CrossRef]
19. Lee, J.S.; Pottier, E. *Polarimetric Radar Imaging: From Basics to Applications*; Number 142 in Optical Science and Engineering; CRC Press: Boca Raton, FL, USA, 2009.
20. Richards, M.A.; Scheer, J.; Holm, W.A. *Principles of Modern Radar*; SciTech Pub: Raleigh, NC, USA, 2010.

21. Villano, M.; Papathanassiou, K.P.; Krieger, G.; Moreira, A. Imaging a Wide Swath with Full Polarimetry. In Proceedings of the POLINSAR 2015, Frascati, Italy, 26–30 January 2015; Volume 729, p. 3.
22. Ho Tong Minh, D.; Toan, T.L.; Rocca, F.; Tebaldini, S.; d'Alessandro, M.M.; Villard, L. Relating P-Band Synthetic Aperture Radar Tomography to Tropical Forest Biomass. *IEEE Trans. Geosci. Remote Sens.* **2014**, *52*, 967–979. [CrossRef]
23. Sai Bharadwaj, P.; Kumar, S.; Kushwaha, S.P.S.; Bijker, W. Polarimetric scattering model for estimation of above ground biomass of multilayer vegetation using ALOS-PALSAR quad-pol data. *Phys. Chem. Earth Parts A/B/C* **2015**, *83–84*, 187–195. [CrossRef]
24. Eini-Zinab, S.; Maghsoudi, Y.; Sayedain, S.A. Assessing the performance of indicators resulting from three-component Freeman–Durden polarimetric SAR interferometry decomposition at P-and L-band in estimating tropical forest aboveground biomass. *Int. J. Remote Sens.* **2020**, *41*, 433–454. [CrossRef]
25. Waqar, M.M.; Sukmawati, R.; Ji, Y.Q.; Sri Sumantyo, J.T.; Segah, H.; Prasetyo, L.B. Retrieval of tropical peatland forest biomass from polarimetric features in central Kalimantan, Indonesia. *Prog. Electromagn. Res. C* **2020**, *98*, 109–125. [CrossRef]
26. Watanabe, M.; Shimada, M.; Rosenqvist, A.; Tadono, T.; Matsuoka, M.; Romshoo, S.; Ohta, K.; Furuta, R.; Nakamura, K.; Moriyama, T. Forest Structure Dependency of the Relation Between L-Bandsigma^0 and Biophysical Parameters. *IEEE Trans. Geosci. Remote Sens.* **2006**, *44*, 3154–3165. [CrossRef]
27. El Moussawi, I.; Ho Tong Minh, D.; Baghdadi, N.; Abdallah, C.; Jomaah, J.; Strauss, O.; Lavalle, M.; Ngo, Y.N. Monitoring Tropical Forest Structure Using SAR Tomography at L- and P-Band. *Remote Sens.* **2019**, *11*, 1934. [CrossRef]
28. Ngo, Y.N.; Huang, Y.; Minh, D.H.T.; Ferro-Famil, L.; Fayad, I.; Baghdadi, N. Tropical Forest Vertical Structure Characterization: From GEDI to P-Band SAR Tomography. *IEEE Geosci. Remote Sens. Lett.* **2022**, *19*, 1–5. [CrossRef]
29. Trudel, M.; Magagi, R.; Granberg, H.B. Application of Target Decomposition Theorems Over Snow-Covered Forested Areas. *IEEE Trans. Geosci. Remote Sens.* **2009**, *47*, 508–512. [CrossRef]
30. Antropov, O.; Rauste, Y.; Hame, T. Volume Scattering Modeling in PolSAR Decompositions: Study of ALOS PALSAR Data Over Boreal Forest. *IEEE Trans. Geosci. Remote Sens.* **2011**, *49*, 3838–3848. [CrossRef]
31. Hu, Y.; Nie, Y.; Liu, Z.; Wu, G.; Fan, W. Improving the Potential of Coniferous Forest Aboveground Biomass Estimation by Integrating C- and L-Band SAR Data with Feature Selection and Non-Parametric Model. *Remote Sens.* **2023**, *15*, 4194. [CrossRef]
32. Sandberg, G.; Ulander, L.M.H.; Wallerman, J.; Fransson, J.E.S. Measurements of Forest Biomass Change Using P-Band Synthetic Aperture Radar Backscatter. *IEEE Trans. Geosci. Remote Sens.* **2014**, *52*, 6047–6061. [CrossRef]
33. Huuva, I.; Persson, H.J.; Soja, M.J.; Wallerman, J.; Ulander, L.M.H.; Fransson, J.E.S. Predictions of Biomass Change in a Hemi-Boreal Forest Based on Multi-Polarization L- and P-Band SAR Backscatter. *Can. J. Remote Sens.* **2020**, *46*, 661–680. [CrossRef]
34. Huuva, I.; Persson, H.J.; Wallerman, J.; Ulander, L.M.; Fransson, J.E.S. Prediction of Hemi-Boreal Forest Biomass Change Using Alos-2 Palsar-2 L-Band SAR Backscatter. In Proceedings of the IGARSS 2023—2023 IEEE International Geoscience and Remote Sensing Symposium, Pasadena, CA, USA, 16–21 July 2023; pp. 3326–3329. ISSN: 2153-7003. [CrossRef]
35. Freeman, A.; Durden, S.L. Three-component scattering model to describe polarimetric SAR data. In Proceedings of the SPIE, San Diego, CA, USA, 13 July 1993; Volume 1748, pp. 213–224. [CrossRef]
36. Freeman, A.; Durden, S.L. A three-component scattering model for polarimetric SAR data. *IEEE Trans. Geosci. Remote Sens.* **1998**, *36*, 963–973. [CrossRef]
37. Shriniwas, A. Polarimetric Decomposition of SAR Data for Forest Structure Assessment. Masters Thesis, Chalmers Technical University, Goteborg, Sweden, 2013.
38. Nguyen, L.V.; Tateishi, R.; Nguyen, H.T.; Sharma, R.C.; To, T.T.; Le, S.M. Estimation of Tropical Forest Structural Characteristics Using ALOS-2 SAR Data. *Adv. Remote Sens.* **2016**, *5*, 131–144. [CrossRef]
39. Adeli, S.; Salehi, B.; Mahdianpari, M.; Quackenbush, L.J.; Chapman, B. Moving Toward L-Band NASA-ISRO SAR Mission (NISAR) Dense Time Series: Multipolarization Object-Based Classification of Wetlands Using Two Machine Learning Algorithms. *Earth Space Sci.* **2021**, *8*, e2021EA001742. [CrossRef]
40. Liu, Z.; Michel, O.O.; Wu, G.; Mao, Y.; Hu, Y.; Fan, W. The Potential of Fully Polarized ALOS-2 Data for Estimating Forest Above-Ground Biomass. *Remote Sens.* **2022**, *14*, 669. [CrossRef]
41. Avtar, R.; Sawada, H.; Takeuchi, W.; Singh, G. Characterization of forests and deforestation in Cambodia using ALOS/PALSAR observation. *Geocarto Int.* **2012**, *27*, 119–137. [CrossRef]
42. Zhang, L.; Zhang, J.; Zou, B.; Zhang, Y. Comparison of Methods for Target Detection and Applications Using Polarimetric SAR Image. In Proceedings of the PIERS Proceedings 2008, Hangzhou, China, 2–6 July 2008; pp. 294–299.
43. Kim, Y.; van Zyl, J. On the relationship between polarimetric parameters. In Proceedings of the IEEE 2000 International Geoscience and Remote Sensing Symposium, Honolulu, HI, USA, 24–28 July 2000; Volume 3, pp. 1298–1300. [CrossRef]
44. Ling, F.; Li, Z.; Chen, E.; Wang, Q. Comparison of ALOS PALSAR RVI and Landsat TM NDVI for forest area mapping. In Proceedings of the 2009 2nd Asian-Pacific Conference on Synthetic Aperture Radar, 26–30 October 2009; pp. 132–135. [CrossRef]
45. Kim, Y.; Jackson, T.; Bindlish, R.; Lee, H.; Hong, S. Radar Vegetation Index for Estimating the Vegetation Water Content of Rice and Soybean. *IEEE Geosci. Remote Sens. Lett.* **2012**, *9*, 564–568. [CrossRef]
46. Jin, X.; Yang, G.; Xu, X.; Yang, H.; Feng, H.; Li, Z.; Shen, J.; Lan, Y.; Zhao, C. Combined Multi-Temporal Optical and Radar Parameters for Estimating LAI and Biomass in Winter Wheat Using HJ and RADARSAR-2 Data. *Remote Sens.* **2015**, *7*, 13251–13272. [CrossRef]

47. Szigarski, C.; Jagdhuber, T.; Baur, M.; Thiel, C.; Parrens, M.; Wigneron, J.P.; Piles, M.; Entekhabi, D. Analysis of the Radar Vegetation Index and Potential Improvements. *Remote Sens.* **2018**, *10*, 1776. [CrossRef]
48. Marklund, L. *Biomass Functions for Pine, Spruce and Birch in Sweden*; Swedish National Forest Inventory: Umeå, Sweden, 1988.
49. Fuller, R.M.; Smith, G.M.; Devereux, B.J. The characterisation and measurement of land cover change through remote sensing: Problems in operational applications? *Int. J. Appl. Earth Obs. Geoinf.* **2003**, *4*, 243–253. [CrossRef]
50. McRoberts, R.E.; Næsset, E.; Gobakken, T.; Bollandsås, O.M. Indirect and direct estimation of forest biomass change using forest inventory and airborne laser scanning data. *Remote Sens. Environ.* **2015**, *164*, 36–42. [CrossRef]
51. Lee, J.S.; Ainsworth, T.L.; Wang, Y.; Chen, K.S. Polarimetric SAR Speckle Filtering and the Extended Sigma Filter. *IEEE Trans. Geosci. Remote Sens.* **2015**, *53*, 1150–1160. [CrossRef]
52. Cartus, O.; Santoro, M.; Wegmüller, U.; Rommen, B. Benchmarking the Retrieval of Biomass in Boreal Forests Using P-Band SAR Backscatter with Multi-Temporal C- and L-Band Observations. *Remote Sens.* **2019**, *11*, 1695. [CrossRef]
53. Ratha, D.; Mandal, D.; Kumar, V.; Mcnairn, H.; Bhattacharya, A.; Frery, A.C. A Generalized Volume Scattering Model-Based Vegetation Index From Polarimetric SAR Data. *IEEE Geosci. Remote Sens. Lett.* **2019**, *16*, 1791–1795. [CrossRef]
54. Ahmed, R.; Siqueira, P.; Hensley, S.; Chapman, B.; Bergen, K. A survey of temporal decorrelation from spaceborne L-Band repeat-pass InSAR. *Remote Sens. Environ.* **2011**, *115*, 2887–2896. [CrossRef]
55. Lavalle, M.; Hensley, S. Extraction of Structural and Dynamic Properties of Forests From Polarimetric-Interferometric SAR Data Affected by Temporal Decorrelation. *IEEE Trans. Geosci. Remote Sens.* **2015**, *53*, 4752–4767. [CrossRef]